1 # How does the phytoplankton-light feedback affect the marine N_2O inventory?

3 Sarah Berthet [1*], Julien Jouanno [2], Roland Séférian [1], Marion Gehlen [3], William Llovel [4]
4 [1] CNRM, Université de Toulouse, Météo-France, CNRS, Toulouse, France
5 [2] LEGOS, Université de Toulouse, IRD, CNRS, CNES, UPS, Toulouse, France
6 [3] LSCE, Université Paris-Saclay, Institut Pierre Simon Laplace, Gif-Sur-Yvette, France
7 [4] LOPS, CNRS/University of Brest/IFREMER/IRD, Brest, France
8
9 ([*]correspondence: sarah.berthet@meteo.fr)

Abstract
11

13 The phytoplankton-light feedback (PLF) describes the interaction between phytoplankton
14 biomass and the downwelling shortwave radiation entering the ocean. The PLF allows to
15 simulate differential heating across the ocean water column as a function of phytoplankton
16 concentration. Only one third of the Earth system models contributing to the 6th phase of the
17 Coupled Model Intercomparison Project (CMIP6) includes a complete representation of the
18 PLF. In other models, the PLF is approximated either by a prescribed climatology of chlorophyll
19 or not represented at all. Consequences of an incomplete representation of the PLF on the
20 modelled biogeochemical state have not yet been fully assessed and remain a source of multi-
21 model uncertainty in future projection. Here, we evaluate within a coherent modelling
22 framework how representations of the PLF of varying complexity impact ocean physics and
23 ultimately marine production of nitrous oxide (N_2O), a major greenhouse gas. We exploit global
24 sensitivity simulations at 1-degree of horizontal resolution over the last two decades (1999-
25 2018) coupling ocean, sea ice and marine biogeochemistry. The representation of the PLF
26 impacts ocean heat uptake and temperature of the first 300 meters of the tropical ocean.
27 Temperature anomalies due to an incomplete PLF representation drive perturbations of ocean
28 stratification, dynamics and oxygen concentration. These perturbations translate into different
29 projection pathways for N_2O production depending on the choice of the PLF representation.
30 The oxygen concentration in the North Pacific oxygen minimum zone is overestimated in model
31 runs with an incomplete representation of the PLF which results in an underestimation of local
32 N_2O production. This leads to important regional differences of sea-to-air N_2O fluxes: fluxes are
33 enhanced by up to 24% in the south Pacific and south Atlantic subtropical gyres, but reduced
34 by up to 12% in oxygen minimum zones of the northern hemisphere. Our results based on a
35 global ocean-biogeochemical model at CMIP6 state-of-the-art shed light on current
36 uncertainties in modelled marine nitrous oxide budgets in climate models.

37

Plain language summary
38
39

40 Phytoplankton absorbs the solar radiation entering the ocean surface, and contributes to keep
41 the associated energy in surface waters. This natural effect is either not represented in the
42 ocean component of climate models, or in a simplified manner. We show that an incomplete
43 representation of this biophysical interaction affects the way climate models simulate ocean
44 warming, which leads to uncertainties in projections of oceanic emissions of an important
45 greenhouse gas called the nitrous oxide.

46

Key-words: phytoplankton-light interaction; bio-physical feedback; nitrous oxide; N$_2$O; CMIP6 Earth system models; CNRM-ESM2-1; ocean-biogeochemical model; greenhouse gazes; marine emission; climate

Key points:
- forced ocean-biogeochemical simulations reveal that marine production of nitrous oxide is sensitive to the representation of the phytoplankton-light feedback
- the phytoplankton-light feedback perturbs the accumulation of heat and the ocean dynamics which drive changes in nitrous oxide production patterns
- an incomplete phytoplankton-light feedback overestimates sea-to-air N$_2$O fluxes by up to 24% in subtropical gyres and reduces them by up to 12% in oxygen minimum zones

1. Introduction

Feedbacks between the physical, biogeochemical, or ecosystem components of the ocean can trigger abrupt system changes (Heinze et al., 2021). At present the interactive phytoplankton-light feedback (PLF) is the only coupling in Earth system models between modelled marine biogeochemistry and ocean dynamics (Séférian et al., 2020). It implies that the chlorophyll (CHL) produced by the biogeochemical model is used to determine the fraction of shortwave radiation penetrating ocean surface waters. In this case, the CHL concentration profile used to approximate the influence of plankton biomass on the vertical redistribution of heat in the upper ocean is consistent with the one used to compute biogeochemical cycling.

a) Phytoplankton-light feedback (PLF)

Since the first observational evidence on how suspended matter in surface waters will impact light absorption by the ocean and change the radiative imbalance within the mixed layer (Kahru et al. 1993), this biophysical interaction has been gradually included to ocean models. Gildor and Naik (2005) highlighted the importance of considering monthly variations of CHL to capture the first-order effect of marine biota on light penetration in ocean models. Adding light-CHL interactions to numerical simulations affects oceanic processes over a wide range of spatial and temporal scales. Enabling a phytoplankton-light interaction modifies the hydrodynamics of the water column (Edwards et al., 2001; Edwards et al., 2004), the intensity of the spring-bloom in subpolar regions (Oschlies, 2004), the maintenance of the Pacific Cold Tongue (Anderson et al., 2007), the seasonality of the Arctic Ocean (Lengaigne et al., 2009), the strength of the tropical Pacific annual cycle, as well as the ENSO variability (Timmermann and Jin, 2002; Marzeion et al., 2005), the northward extension of the meridional overturning circulation (Patara et al., 2012) and the cooling of the Atlantic and Peru-Chili upwelling systems (Hernandez et al., 2017, Echevin et al., 2022).

However, the mean effect of the PLF on sea surface temperature has been argued to depend on the numerical framework (forced ocean versus coupled ocean-atmosphere models). The conflicting results reported in the literature were mainly due to diverging bio-optical protocols among models rather than to the inclusion of air-sea coupling. According to Park et al. (2014) atmosphere-ocean coupling amplifies the magnitude of PLF-induced changes, without altering the sign of the response obtained in ocean-only simulations. Two main causes were put forward

to explain the sign of the final heat perturbation: either an indirect dynamical response (Murtugudde et al., 2002; Löptien et al., 2009) or a direct thermal effect (Mignot et al., 2013; Hernandez et al., 2017). Hernandez et al. (2017) further distinguished a local from a remote thermal effect by highlighting the important role played by the advection of offshore CHL-induced cold anomalies in the Benguela upwelling waters. The interplay of these mechanisms is regionally variable (Park et al., 2014). Despite the diversity of modelled responses, a consensus emerges on the first order effect of PLF on the ocean physics, which is to perturb the ocean thermal structure (Nakamoto et al., 2001; Murtuggude et al., 2002; Oschlies, 2004; Manizza et al., 2005, 2008; Anderson et al., 2007; Lengaigne et al., 2007; Gnanadesikan and Anderson, 2009; Löptien et al., 2009; Patara et al., 2012; Mignot et al., 2013; Hernandez et al., 2017). By trapping more heat at the ocean surface in eutrophic regions, such as coastal or equatorial upwellings areas, the presence of phytoplankton initially increases the surface warming. Confining heat at the surface leads to less heat penetrating in subsurface. In some cases, the advection and upwelling of subsurface cold anomalies can lead to remote cooling effects (Hernandez et al., 2017; Echevin et al., 2022). Dynamical readjustment in response to perturbations in thermal structure has also been shown to have a cooling effect, by increasing upwelling of cold water to the ocean surface (Manizza et al. 2005; Marzeion et al., 2005; Nakamoto et al., 2001; Löptien et al., 2009; Lengaigne et al., 2007; Park et al., 2014). Because these effects depend on upper ocean stratification, an important role is attributed to modelled seasonal deepening of the mixed layer as it determines the intensity of the underlying temperature anomaly and its vertical movement to the surface. In other terms, whatever the temporality of the causal chain, changes in the PLF representation are expected to both perturb the ocean heat uptake, and trigger perturbations of both the water column stratification and associated ocean dynamics.

b) This study: implications for N$_2$O budget uncertainties

Nitrous oxide (N$_2$O) is a major ozone-depleting substance (Ravishankara et al., 2009; Freing et al., 2012) and a potent greenhouse gas, whose global warming potential is 265-298 times that of CO$_2$ for a 100-year timescale (Myhre et al., 2013). The spatial coherence between marine productive areas and observed hot-spots of N$_2$O production leads to question the impact of an incomplete representation of the PLF on the simulated N$_2$O inventory. Recent observational studies highlight that N$_2$O production is high in low-oxygen tropical regions and cold upwelling waters (Arévalo-Martinez et al. 2018; 2020; Yang et al., 2020; Wilson et al., 2020). N$_2$O becomes increasingly saturated in surface waters of equatorial upwelling regions due to the upward advection of N$_2$O-rich waters (Arévalo-Martínez et al., 2017). Regions known to account for the most productive areas of the ocean spatially coincide with highest N$_2$O production: 64% of the annual N$_2$O flux occurs in the tropics, and 20% in coastal upwelling systems that occupy less than 3% of the ocean area (Yang et al., 2020).

Despite recent advances, a large range of uncertainties still surrounds oceanic N$_2$O emissions as large areas of both the open and coastal ocean remain undersampled by observations (Wilson et al., 2020). In particular, the paucity of observational data over key source regions contributes to increase uncertainties. The recent global budget of Tian et al. (2020) estimates natural sources from soils and oceans to contribute with up to 57% to the total N$_2$O emissions between 2007 and 2016, with the ocean flux reaching 3.4 (2.5–4.3) Tg N yr^{-1}. A large uncertainty range is associated to the ocean flux estimate, as it is based on outputs from only a small

141 number of global ocean-biogeochemical models. Very few climate models, even in the current
142 CMIP6 generation, include emissions (and beforehand a complete representation of N cycling)
143 of N_2O fluxes: only 4 out of the 26 Earth system models considered in Séférian et al. (2020)
144 simulate marine N_2O emissions.

146 The last generation of Earth system models projects an enhanced ocean warming in response
147 to climate change, which is in turn expected to increase upper-ocean stratification (Sallée et
148 al., 2021) and to contribute to greater reductions in upper-ocean nitrate and subsurface oxygen
149 ventilation (Kwiatkowski et al., 2020). Ocean warming and deoxygenation constitute two
150 triggers of high-probability high-impact climate tipping points (Heinze et al., 2021) and are
151 identified as two of the main environmental factors influencing marine N_2O distributions (IPCC,
152 2019; Hutchins and Capone, 2022). Through its expected impacts on the upper ocean
153 stratification, the PLF representation could further change the oceanic N_2O source by
154 modulating the mixing between N_2O-rich water and intermediate depths, perturbing the way
155 N_2O-rich water reaches the air-sea interface (Freing et al., 2012).

157 Here we investigate how an incomplete representation of the PLF leads to uncertainties in N_2O
158 projection in an up-to-date global ocean-biogeochemical model making up the current
159 generation of Earth system models. Section 2 describes the numerical model and the set of
160 simulations, as well as the existing options to consider CHL modulations of the incoming
161 shortwave radiation. Section 3 presents the effect of an interactive PLF on the ocean heat
162 content, associated ocean stratification and dynamics, and its feedback on marine N_2O
163 inventory. Finally, Section 4 summarizes the main results, addresses their broader implications,
164 and discusses the future work motivated by this study.

166 2. Methodology

168 **a) Configuration of the global ocean-biogeochemical model**

170 Recent projections of future N_2O emissions contributing to intercomparison projects like CMIP6
171 are still based on Earth system models with a low spatial resolution (Séférian et al., 2020). For
172 sake of coherence with CMIP biogeochemical modelling efforts, in the following we use a global
173 ocean-biogeochemical configuration of the NEMO-PISCESv2 model (Madec, 2008; Aumont et
174 al., 2015) at 1° of horizontal resolution. This model corresponds to the oceanic component of
175 CNRM-ESM2-1 (Séférian et al., 2019) and is one of the few CMIP6-class models that contributed
176 to the Global N_2O budget (Tian et al., 2020). Our modelled ocean has 75 vertical levels and the
177 first level is at 0.5 meter depth. Vertical levels are unevenly spaced with 35 levels being in the
178 first 300 meters of depth. Atmospheric forcings of momentum, incoming radiation,
179 temperature, humidity, and freshwater are provided to the ocean surface by bulk formulae
180 following Large and Yeager (2009). Details on physical configuration are given in Berthet et al.
181 (2019). Using an ocean-only configuration allows to isolate the local response induced by the
182 PLF by not confounding it with potential inter-basin feedbacks acting through the atmosphere.

184 JRA55-do atmospheric reanalysis (Tsujino et al., 2018; Tsujino et al., 2020) provided the
185 atmospheric forcings of the ocean. The global domain was first spun-up under preindustrial
186 conditions during several hundred years ensuring that all fields approached a quasi-steady
187 state. The historical evolution of atmospheric CO_2 and N_2O concentrations was prescribed since

188   1850. To avoid the warming jump between the end of the spin-up and the onset of the
189   reanalyses in 1958, the first 5 years of JRA55-do forcings were cycled, followed by the complete
190   period of JRA55-do atmospheric forcing from 1958 to 2018.
191
192   **b) Experimental design: three representations of the PLF**
193
194   The control simulation (hereafter REF) together with the spin-up both account for a fully
195   interactive PLF: the penetration of shortwave radiation into the ocean surface is constrained
196   by the CHL concentration ([CHL]) produced by the PISCESv2 biogeochemical component (Figure
197   S1, REF).
198
199   PISCESv2 (Pelagic Interactions Scheme for Carbon and Ecosystem Studies v2) is a 3D
200   biogeochemical model which simulates the lower trophic levels of marine ecosystems
201   (nanophytoplankton, diatoms, microzooplankton and mesozooplankton), the biogeochemical
202   cycles of carbon and of the main nutrients (phosphate, nitrogen, iron, and silicate) along the
203   75 levels of our numerical ocean. A comprehensive presentation of the model is found in
204   Aumont et al. (2015). PISCESv2 simulates prognostic 3D distributions of nanophytoplankton
205   and diatom concentrations. The evolution of phytoplankton biomasses is the net outcome of
206   growth, mortality, aggregation and grazing by zooplankton. Growth rate of phytoplankton
207   mainly depends on the length of the day, depths of the mixed layer and of the euphotic zone,
208   the mean residence time of the cells within the unlit part of the mixed layer and includes a
209   generic temperature dependency (Eppley, 1972). Nanophytoplankton growth depends on the
210   external nutrient concentrations in nitrogen and phosphate (Monod-like parameterizations of
211   N and P limitations), and on Fe limitation which is modeled according to a classical quota
212   approach. The production terms for diatoms are defined as for nanophytoplankton, except that
213   the limitation terms also include silicate.
214
215   Light absorption by phytoplankton depends on the waveband and on the species (Bricaud et
216   al., 1995). A simplified formulation of light absorption by the ocean is used in our experiments
217   to calculate both the phytoplankton light limitation in PISCESv2 and the oceanic heating rate
218   (Lengaigne et al., 2007). In this formulation, visible light is split into three wavebands: blue
219   (400–500 nm), green (500–600 nm) and red (600–700 nm); for each waveband, the CHL-
220   dependent attenuation coefficients, k_R, k_G and k_B, are derived from the formulation proposed
221   in Morel and Maritorena (2001):
222

223   $$k_{WLB} = \sum_{\lambda_1}^{\lambda_2} \left(k(\lambda) + \chi(\lambda)[\text{CHL}]^{e(\lambda)} \right) \qquad (1)$$

224   where WLB means the wavelength band associated to red (R), green (G) or blue (B), and
225   bounded by the wavelengths λ_1 and λ_2 as detailed above. $k(\lambda)$ is the attenuation coefficient
226   for optically pure sea water. $\chi(\lambda)$ and $e(\lambda)$ are fitted coefficients which allows to determine
227   the attenuation coefficients due to chlorophyll pigments in sea water (Morel and Maritorena,
228   2001).
229
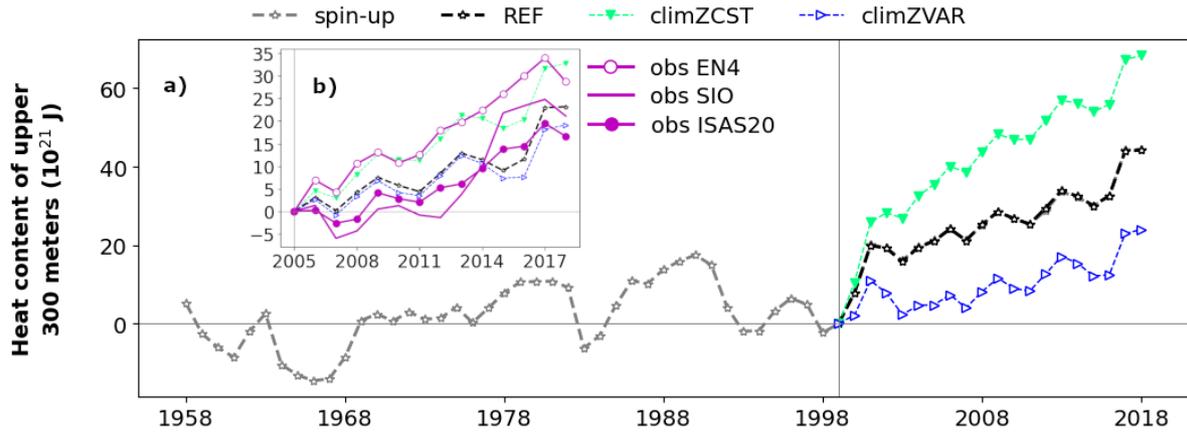
230

231 Figure 1: Modelled tropical [35°S-35°N] heat content of upper 300 m (OHC300; in ZJ) for each
232 simulation described in Table 1: REF (black; empty stars), climZCST (green; full downward
233 triangles) and climZVAR (blue; empty rightward triangles). In (a) final part of the spin-up has
234 been added in gray to illustrate the branching protocol in year 1999, and OHC300 anomalies
235 have been computed with respect to year 1999. Subplot (b) zooms over the Argo period to
236 compare modelled tropical OHC300 anomalies with 3 in situ-based products (see section 2c).

237

238 At year 1999 two sensitivity experiments were branched off (Figure 1). Both simulations
239 climZCST and climZVAR account for an incomplete and external PLF, as they consider an
240 observed climatology of surface [CHL] from ESACCI (Valente et al., 2016) in order to compute
241 the light penetration into sea water (Equation 1; Figure S1). These two simulations differ from
242 each other by the "realism" of the vertical profile derived in each grid point from the surface
243 value of the ESACCI CHL climatology to the level of light extinction (Table 1). climZCST uses
244 constant profiles of CHL spreading uniformly in the vertical direction (Figure 2, b and d-f).
245 climZVAR uses variable vertical profiles computed following Morel and Berthon (1989) (Figure
246 2, c and d-f). This set of simulations is representative of the several configurations used in the
247 case of CMIP intercomparison project.

248

249 Table 1: Experimental set-up.

250

Simulation	Which CHL fields to interact with incoming shortwave radiation?	PLF nature
REF	uses directly the 3D CHL produced by the biogeochemical component	interactive
climZCST	uses the prescribed monthly climatology of ESACCI CHL with a constant vertical profile, equal to the value of the surface climatology up to the level of light extinction	incomplete
climZVAR	uses the prescribed monthly climatology of ESACCI CHL with a variable vertical profile, derived from the surface climatology following Morel and Berthon (1989)	incomplete

251
252

253 In climZCST and climZVAR, PISCESv2 prognostically simulates [CHL], a key component of
254 biogeochemical cycles, but feedback of CHL on physics (stratification, ocean heat content) is
255 determined by the externally prescribed [CHL] climatology. The CHL concentrations used for
256 radiation or for biogeochemical cycles are not consistent, and phytoplankton biomass
257 computed by the biogeochemical model does not affect the physical properties of the ocean
258 waters.
259
260 Consequences on the marine biogeochemical mean state of incomplete representations of the
261 PLF are assessed in the following by difference to the control run REF. This methodology allows
262 to evaluate how different levels of realisms and complexity in resolving bio-physical interactions
263 impact the physical and biogeochemical content of the modelled ocean. A complete
264 description of the marine N_2O parameterization used in this model is presented in the
265 supplementary material.
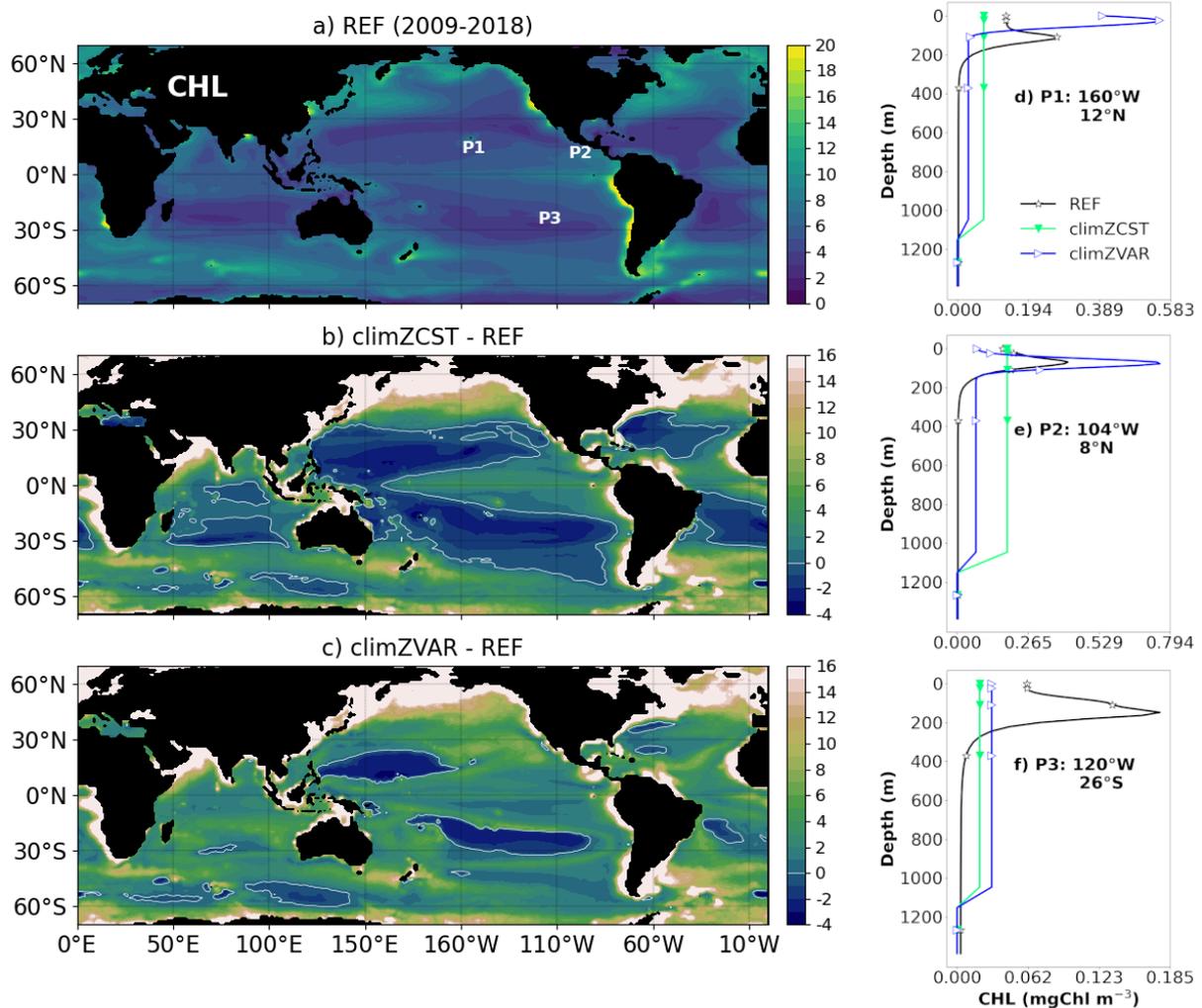
266
267 Figure 2: CHL concentration (mgCHL m^{-3}) interacting with the incoming shortwave radiation for
268 each numerical experiment (Table 1). Maps a-c) show annual means of the vertical sum over 0-
269 6000 m, a) as modelled over the 2009-2018 period for REF, and its differences with the external
270 CHL prescribed for b) climZCST and c) climZVAR experiments. Labels P1 to P3 on subplot a)
271 locate vertical profiles shown on subplots d-f).

272

273

c) Observations and analyses

276 Model results are compared with available observational-based gridded temperature and
277 salinity datasets. Ocean heat content (OHC) of the upper 0-300 meter layer was inferred from
278 three different products: i) the global objective analysis of subsurface temperature EN4 (Good
279 et al., 2013), ii) the SIO product of the Scripps Institution of Oceanography (Roemmich anf
280 Gilson, 2009), and iii) the ISAS20 optimal interpolation product released by Ifremer
281 (Kolodziejczyk et al., 2019; Kolodziejczyk et al., 2021). While the SIO and ISAS20 products
282 consider only Argo temperature and salinity profiles, the EN4 dataset considers all types of *in*
283 *situ* profiles providing temperature and salinity (when available). These three *in situ*-based
284 datasets are considered since 2005, the year the Argo coverage became sufficient to
285 characterize the global ocean. Details on OHC computation are given in Llovel and Terray (2016)
286 and Llovel et al. (2022). The authors also refer to cross-validations of OHC of deeper layers (0-
287 700 m and 0-2000 m) against OHC anomalies from World Ocean Atlas 2009 (Levitus et al.,
288 2012). A monthly climatology (1955-2012) of oceanic temperature from World Ocean Atlas
289 2013 version 2 (Locarnini et al., 2013) was used to evaluate modelled temperatures. Modelled
290 O_2 was compared to the annual climatology of O_2 from World Ocean Atlas 2013 (Garcia et al.,
291 2014) and modelled CHL was compared to the 3D monthly climatological global product
292 estimated from merged satellite and hydrological data of Uitz et al. (2006). Modelled N_2O
293 partial pressure difference across the air-sea interface (Dpn2o) was compared to the recent
294 dataset of Dpn2o observations compiled by Yang et al. (2020).

296 In the following temporal means cover the last 10 years of simulations, from 2009 to 2018. In
297 other analyses the whole simulated period is shown (1999-2018).

3. Results

a) Impact of PLF on the upper ocean heat content and dynamics

303 Meridional sections reveal that heat perturbations in response to changing CHL fields
304 interacting with light are limited to the top 0-300 m layer of the ocean and predominantly affect
305 the tropical area (Figure 3 and Figure S2, c-d).

307 The largest temperature anomalies are observed near the thermocline depth and reflect upper
308 ocean warming and deepening of the thermocline in climZCST (Figure 3c), and cooling and
309 shallowing of the thermocline in climZVAR (Figure 3d). In climZCST the ocean warming reflects
310 large-scale patterns of a tropical CHL deficit compared to REF (Figure 2, b). Temperature
311 differences are lower in the near-surface layer (0-50 m) than in the 50-300 m layer. This is
312 expected as a result from weak stratification but also from simulations run with a forced
313 atmosphere in which the temperature of the ocean surface layer is constrained by the
314 atmospheric prescribed state.

316 When using an incomplete representation of the PLF, two contrasting trends of the upper
317 ocean heat content (OHC) emerge compared to our control run REF (Figure 1a). Over the Argo
318 period (2005-present) EN4 estimates of tropical OHC300 are in very good agreement with our
319 warmest simulation climZCST (Figure 1b), while the two other dataproducts SIO and ISAS20 are

in better agreement with our control run REF and with climZVAR. The good accordance between modeled OHC300 and observations is not a systematic feature of model-data comparisons (Cheng et al., 2016; Liao et al., 2022). Moreover, non-negligible differences exist among OHC dataproducts which are generally particularly strong in the upper 0-300 m layer (Lyman et al., 2010; Liang et al., 2021). The spread between these products at the end of the 2005-2018 period (12.1 10^{21} J) is comparable to that of our numerical set (13.6 10^{21} J). The modelled OHC in REF is in very good agreement with current global mean *in situ* observations (Meyssignac et al., 2019; see their Figure 11) and with OHC anomalies derived from World Ocean Atlas 2009 (Levitus et al., 2012). In accordance with these observations, our ocean-biogeochemical model simulates a global mean increase of OHC over the 2006-2016 period of order 40 10^{21} J for the upper 700 m, and of about 70 10^{21} J for the 0-2000 m layer.
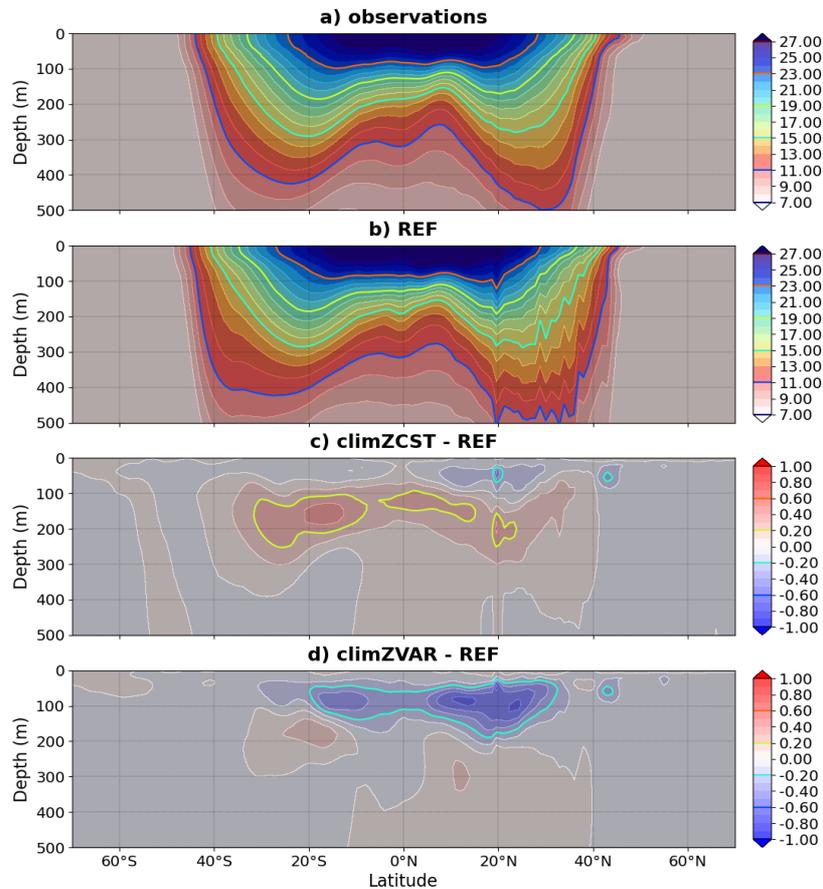
Figure 3: Mean 2009-2018 meridional section of temperature (°C) averaged over 0-360°E for a) observations, b) REF and its differences with c) climZCST and d) climZVAR.

Subsurface thermal anomalies develop rapidly (Figure S3) after branching of climZVAR and climZCST in 1999. The dipole structure of the anomaly seen in climZCST reflects the surface heat trapping in REF and the associated subsurface cooling (Figure S3, b). Indeed in climZCST the vertically constant and weaker concentrations of CHL trap less incoming shortwave than the CHL maximum seen in REF between 0 and 100 m depth (Figure 2, d-f). The negative anomaly in climZVAR suggests that the parameterization of Morel and Berthon (1989) contributes to underestimate the ocean heat uptake (Figure S3, c and Figure S2, d) compared to REF. This heat deficit results from the overestimation of the vertical integral of CHL over large areas of the

342   tropical domain in climZVAR compared to REF (Figure 2, c). As a result, the energy associated
343   with the incoming radiation is caught in surface waters without being distributed over the water
344   column.
345
346   In both climZCST and climZVAR the subsurface temperature anomaly deepens progressively
347   over the first six years of simulation as a result of vertical mixing (Figure S3). This evolution
348   indicates that part of the OHC300 differences between simulations comes from the adjustment
349   of climZCST and climZVAR to the spin-up mean state yielded by an interactive PLF. It can be
350   expected that experiments having spin-ups run with different representations of the PLF, would
351   give even stronger sensitivities than those highlighted in this study. The sensitivities of OHC300
352   to the PLF formulation evaluated here should be considered at the lower end of estimate of
353   OHC discrepancies that may emerge from changing the PLF representation.
354
355   Prescribing a constant vertical profile of CHL (climZCST) to compute the penetration of the
356   radiation into the ocean increases the OHC300 by more than 20 10^{21} J during the last two
357   decades (1999-2018) compared to REF (Figure 1). This rise of OHC300 decreases the vertically-
358   integrated tropical potential density of the upper 300 m at the end of the simulated period by
359   5 kg/m^2 compared to REF (Figure S4). The opposite trend (a reduced OHC300 compared to REF)
360   is simulated with the same state-of-the-art CMIP6 ocean-biogeochemical model when
361   considering a variable vertical profile of CHL (climZVAR). However Figure 1 highlights that the
362   simulation using a consistent CHL for interacting with both incoming shortwave radiation and
363   biogeochemical cyclings (REF) does not amplify one of these two trends, as climZCST and
364   climZVAR surround REF. Average ranges of uncertainties associated with the PLF
365   representation over the extended tropical domain (35°S-35°N) exceed 40 10^{21} J in terms of
366   OHC300 (Figure 1), 4 meters for the thermocline depth and more than 9 kg/m^2 for the
367   vertically-integrated potential density perturbation (Figure S4).
368
369   Similar to OHC300, ranges of uncertainty for the OHC estimates of deeper layers (0-700 m and
370   0-2000 m) also slightly exceed 40 10^{21} J. Such uncertainty ranges are quite important as they
371   are obtained by only changing the PLF representation in a single ocean-biogeochemical model.
372   By comparison and in the context of OMIP protocols, Tsujino et al. (2020) give spreads between
373   CMIP model estimates of the order of 50 10^{21} J for the OHC of the upper 700m after 20 years
374   (please refer to their Figure 24, a-b). Regarding the OHC integrated over the 0-2000m layer,
375   they report an inter-model spread between 50 and 100 10^{21} J, depending on the OMIP protocol
376   considered (see their Figure 24, d-e). The OHC300 uncertainty of 40 10^{21} J triggered by the
377   representation of the PLF in our set of simulations has a comparable order of magnitude than
378   the current spread of multi-model estimations of OHC. The present study suggests that part of
379   the OHC multi-model uncertainty in current climate models may be due to different
380   representations of the phytoplankton-light interaction.
381
382   The heat and associated density perturbations also cause dynamical modifications of upper
383   ocean currents (Figure 4). Absolute differences in upper ocean velocities (average between 0
384   and 300m depth) are between |0.05| and |0.6| cm/s with strongest differences along the
385   equator revealing perturbations of the equatorial undercurrent (Figure 4, b and c). Circulation
386   around the subtropical gyres is also impacted, in particular for the South Pacific subtropical
387   gyre. These modifications of zonal and meridional dynamics spread over the entire tropical
388   latitudes, from 30°S to 30°N, strongly supporting the idea that heat perturbations induced by

different interactions between CHL and incoming shortwave cause non-negligible modifications of the equatorial and tropical ocean dynamics.
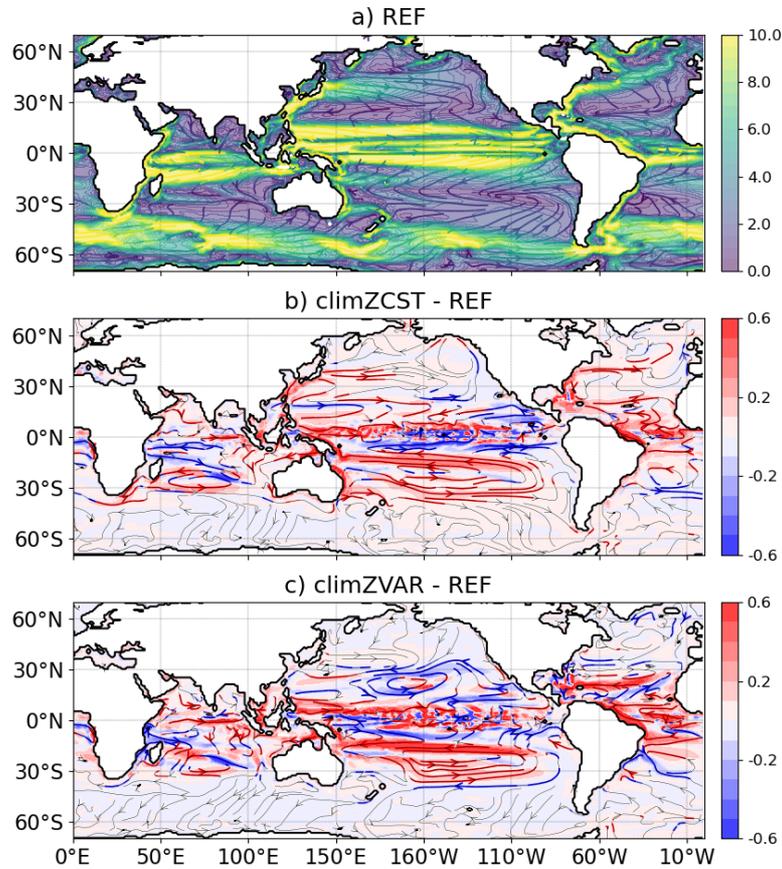
Figure 4: Annual mean speed (color; cm/s) and streamlines of oceanic currents between 0-300 m over the 2009-2018 period for a) REF, and its differences with b) climZCST and c) climZVAR. In b-c) streamlines are colored when absolute speed are larger than 0.05 cm/s.

b) PLF impact on N$_2$O production

Perturbations of the annual pycnocline depth (Figure 5, a-c) highlight a vertical adjustment to the heat (Figure S2) and subsequent large-scale dynamical anomalies (Figure 4). Variations of the pycnocline integrate perturbations of both thermal and salinity stratifications. However, in our simulations heat anomalies appear to drive perturbations and pycnocline depth anomalies mainly reflect those of the thermocline. The cold anomaly dominating the tropical domain in climZVAR (Figure S2, d) appears to be vertically redistributed, as it triggers an upward displacement of the isopycnals (Figure 5, c). In contrast to the anomalies seen over most of the tropical Pacific, a deepening of the isopycnals reaching up to 20 meters is modelled in both South Pacific and Atlantic subtropical gyres in climZCST and climZVAR (Figure 5, b and c). Over these subtropical gyres heat is redistributed along the vertical as the subsurface warm anomaly dives. The subduction of these heat anomalies causes in turn a deepening of the pycnocline (Figure 5, b and c). As stressed by Sweeney et al. (2005), small changes in CHL concentration (Figure S5) may have important effects on the mixed layer depth in these subtropical gyres due to low local wind speeds and low mixing conditions. This is thought to explain the large sensitivity we observe in terms of pycnocline depth (Figure 5) and ocean heat content in these

414 regions. In line with their results, our set of simulations highlights that small CHL changes in low
415 productivity regions trigger a vertical redistribution of density anomalies affecting the
416 stratification.
417
418
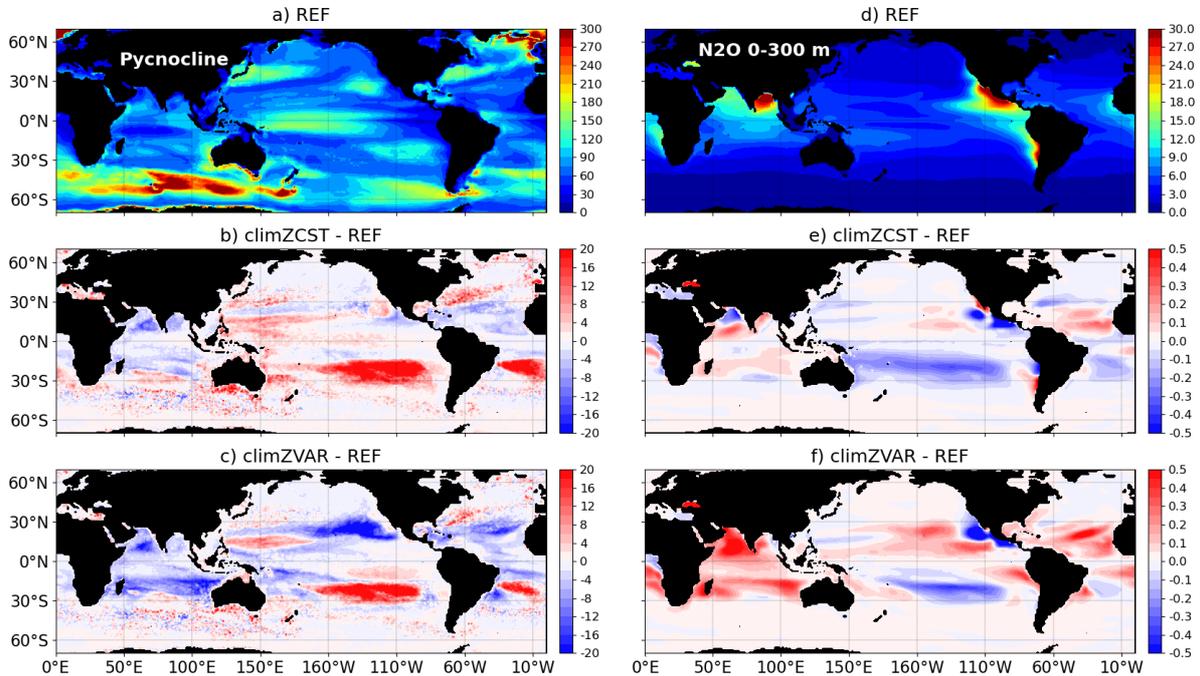
419
420 Figure 5: a-c) Depth of annual pycnocline (m) for 2009-2018 computed as the annual mean
421 depth of the maximum of the Brunt-Väisälä frequency $N^2(T, S)$ over the water column (Maes
422 and O Kane, 2014). d-f) Mean $[N_2O]$ ($\mu molN/m^3$) over the first 300 meters depth. For REF (upper
423 panel) and its mean-state differences with climZCST (middle panel) and climZVAR (bottom
424 panel).
425
426 Anomalies of N_2O concentration integrated over the first 300 meters of the water column
427 (Figure 5, e and f) are in good agreement with patterns of pycnocline anomalies over the tropics
428 (Figure 5, b and c). These comparable spatial structures attest that N_2O anomalies are driven
429 by perturbations of stratification in large parts of the tropical domain.
430
431 In the South Pacific subtropical gyre, the concomitance of i) an increased temperature (Figure
432 S2, c and d), ii) a reinforced transport (Figure 4, b and c) and iii) a weakened stratification
433 illustrated by a local deepening of the pycnocline (Figure 5, b and c), contributes to decrease
434 the N_2O concentration in both climZCST and climZVAR (Figure 5, e and f). In contrast, in the
435 South Indian Ocean and North tropical Atlantic the increase of N_2O concentration seems to be
436 mainly driven by the mean shoaling of the local pycnocline, as both regions exhibit contrasted
437 perturbations in terms of transport and temperature. Finally, in the North Pacific oxygen
438 minimum zone, the strong N_2O deficits in both climZCST and climZVAR compared to REF do not
439 respond to stratification and transport anomalies but are rather driven by a local rise of O_2
440 concentration (Figure S6). Considering an incomplete PLF contributes to overestimate the
441 oxygen concentration in this oxygen minimum zone and leads to a lack of local N_2O production.
442
443 The relationship between N_2O concentration and OHC300 in the Tropical Ocean is derived from
444 a linear regression for each of the three 20-years simulations (Figure 6). The resulting slopes

445   allow to identify three distinct tropical N_2O production pathways along time as a function of
446   the oceanic heat uptake: from 0.3 µmolN m^{-2} per ZJ for the most simplified PLF scenario
447   climZCST, to 1 µmolN m^{-2} per ZJ for climZVAR. The slope of the simulation with the higher level
448   of realism in terms of interactivity (REF) appears a solution between the two previous extremes,
449   as it increases its N_2O production by 0.8 µmolN m^{-2} per ZJ. Each of these N_2O production
450   pathways will translate into a different temporal evolution of the N_2O budget and hence future
451   climate. This result stresses the importance of having an interactive PLF in order to neither
452   overestimate nor underestimate the N_2O production projections due to a simplified
453   representation of the PLF.
454
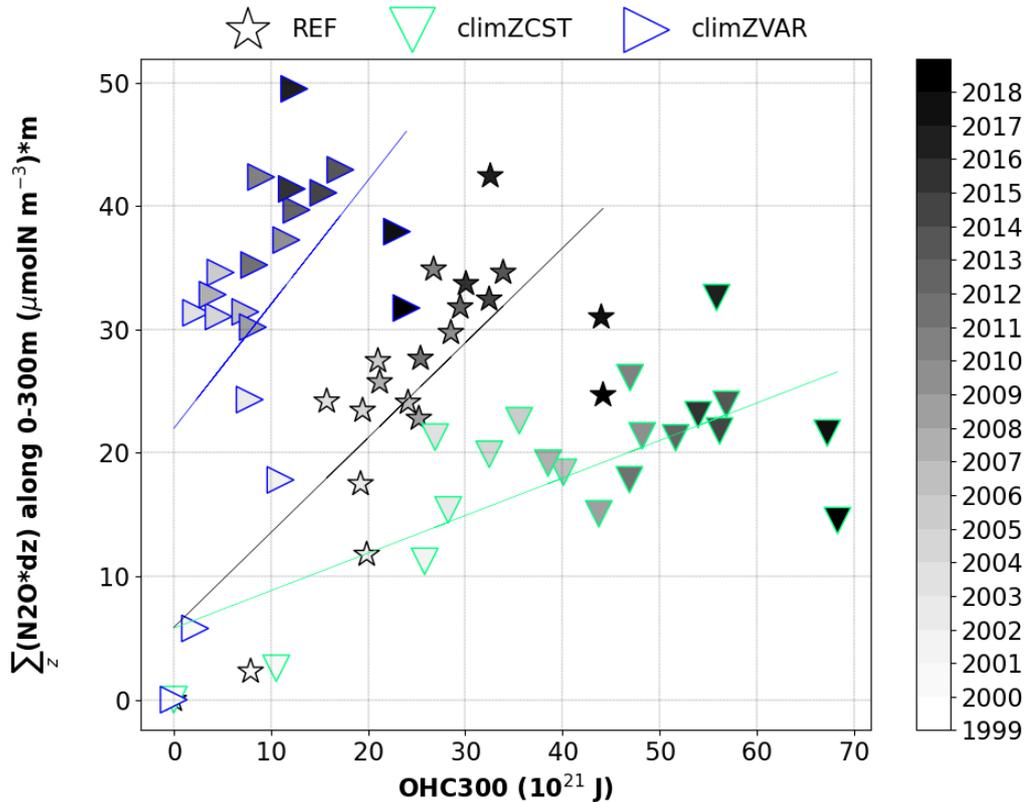
455
456   Figure 6: Annual N_2O inventory vertically integrated over the first 300 meters depth
457   (µmolN/m^2) as a function of the annual OHC300 (ZJ) and averaged over an extended tropical
458   domain (35°S-35°N). All points reflect anomalies compared to year 1999.

459
460   **c) Impacts on oceanic N_2O emissions**

461
462   By perturbing the OHC, the ocean dynamics and the N_2O production, the way PLF is modelled
463   has non-negligible consequences on Dpn2o and thus on N_2O emissions at the air-sea interface
464   (Figure 7). Because the atmospheric partial pressure of N_2O is identical among simulations,
465   differences in Dpn2o are driven by changes in surface oceanic N_2O concentration normalized
466   by those in N_2O solubility. Since solubility is mainly driven by temperature and because surface
467   temperature anomalies are very weak (Figure S3, c and d), we do not expect solubility
468   perturbations close to the surface. It results that spatial patterns of Dpn2o anomalies (Figure
469   7) reflect differences in surface oceanic N_2O concentration.

470

471   Compared to a scenario considering a fully interactive PLF (REF), an incomplete representation
472   of the PLF underestimates Dpn2o in all oxygen minimum zones of the northern hemisphere,
473   which are strong emission zones (Figure 7, c and d). Large Dpn2o anomalies of -2.5 natm
474   encompasses northern parts of the oxygen minimum zones of the Indian, Pacific and Atlantic
475   oceans and anomalies reach up to -5 natm locally. Consequently, climZCST and climZVAR
476   underestimate N_2O fluxes by more than 12% in these oxygen minimum regions compared to
477   REF. This result highlights that the representation of the PLF can be an important source of
478   uncertainty in modelling N_2O fluxes. As a matter of fact, the oceanic contribution to the recent
479   global N_2O budget by Tian et al. (2020) is based on only five global ocean-biogeochemical
480   models (as still only few models simulate marine N_2O emissions). These models have different
481   configurations of the PLF which adds considerable uncertainty to simulated marine N_2O
482   emissions.

483

484   In subtropical gyres, the strong and direct effect of temperature (Figure S2, c and d) on in-depth
485   N_2O concentration (Figure 5, e and f) is in line with Yang et al. (2020) who demonstrate that the
486   seasonality of Dpn2o in that regions is driven by a solubility regime. Both climZCST and
487   climZVAR overestimate Dpn2o in subtropical gyres of the South Pacific and South Atlantic
488   (Figure 7, c and d). This leads to an overestimation of the regional N_2O fluxes by 24% compared
489   to a simulation having a complete and interactive PLF representation (REF).

490
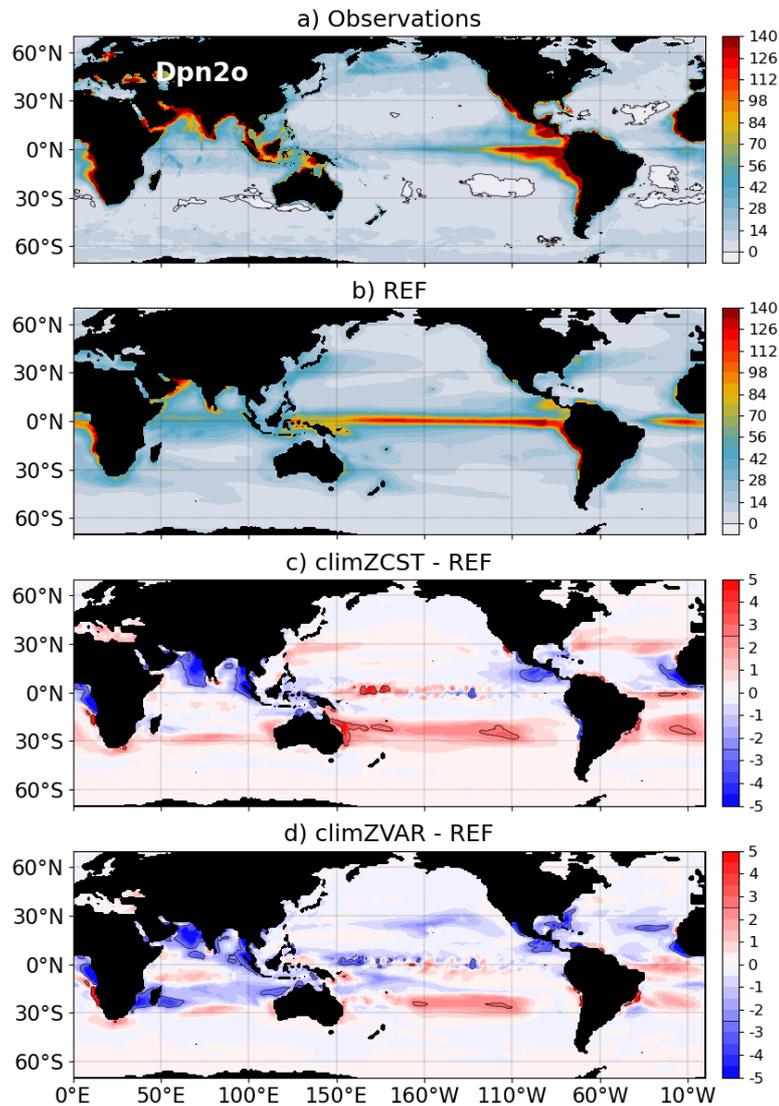
Figure 7: Mean sea-to-air Dpn2o (natm) computed from a) observations, b) REF over the 2009-2018 period, and its differences with c) climZCST and d) climZVAR compared to REF.

4. Discussion and conclusion

In this study we use the ocean component (including ocean physics, sea ice and marine biogeochemistry) of the global Earth system model CNRM-ESM2-1 which contributed to the last phase of the Coupled Model Intercomparison Project (CMIP6). Our ocean-biogeochemical model is one of the few currently able to represent an interactive phytoplankton-light feedback (PLF) by constraining the penetration of shortwave radiation into the ocean as a function of the CHL concentration produced by the biogeochemical model. Three simulations have been run at the horizontal resolution currently used for intercomparisons of Earth system models (1°). Analyses are based on differences between a control run with an interactive PLF (REF) and two experiments with an incomplete PLF (climZCST and climZVAR) using a prescribed CHL climatology to interact with the incoming solar radiation. Changing the approach to compute how CHL filters the light penetrating into the ocean highlights the consequences of using an interactive PLF.

510 Our results demonstrate that the approach commonly used to account for the impact of the
511 phytoplankton on light penetration significantly interfers with upper ocean heat uptake (Figure
512 1), the associated dynamics (Figure 4) and stratification in the tropics (Figure 5, a-c). Our set of
513 forced ocean-biogeochemical simulations reveals that marine production of nitrous oxide
514 (N_2O) is sensitive to the representation of the PLF (Figure 5, d-f). The heat perturbations add to
515 the uncertainty of modelled oceanic N_2O production and result in three N_2O production
516 trajectories along time (Figure 6) that in turn trigger regional differences of Dpn2o and sea-air
517 N_2O fluxes (Figure 7). Compared to an ocean model using a fully interactive PLF (REF), an
518 incomplete PLF results in an overestimation of N_2O fluxes by up to 24% in the South Pacific and
519 South Atlantic subtropical gyres, and a reduction by up to 12% in oxygen minimum zones of the
520 northern hemisphere. Our results based on a model at CMIP6 state-of-the-art emphasize an
521 overlooked important source of uncertainty in climate projections of marine N_2O production
522 and in current estimations of the marine nitrous oxide budget.

524 In subtropical gyres of the southern Hemisphere which are regions of low productivity, small
525 CHL changes have a strong and direct effect on temperature (Figure S2, c and d), transport
526 (Figure 4, b and c) and local stratification (Figure 5, b and c). These concomittant effects result
527 in a local decrease of N_2O concentrations in both experiments with a simplified PLF
528 representation (climZCST and climZVAR).

530 In forced ocean simulations, atmospheric forcings constrain surface temperature, salinity and
531 thus solubility. However, the N_2O concentration integrated over the upper 300 meters depth
532 of the water column (Figure 5, e-f) showed differences with the control run that follow those
533 of the in-depth temperature (Figure S2, c-d): in climZCST (climZVAR), a warmer (colder) tropical
534 ocean leads to a decreased (an increased) N_2O concentration. Because higher marine
535 greenhouse gas emissions will increase the temperature of the coupled atmosphere-ocean
536 system, adding an interactive atmospheric component is expected to amplify the PLF-induced
537 mean changes in marine N_2O concentration highlighted in this ocean-only numerical set (Park
538 et al., 2014; Asselot et al., 2022).

540 Our results also question the reliability of current modelled estimates of the area and volume
541 of oxygen minimum zones, as well as their trends in a future climate. The expansion rate of O_2-
542 depleted waters still remains unclear and its controlling mechanisms are not yet fully
543 understood and represented in today's models. Observation based assessments suggested that
544 the ocean has already lost around 2% of the global marine oxygen since 1960 (Schmidtko et al.,
545 2017). The expansion of oxygen minimum zones is expected to result in an increase of the
546 volume of suboxic water and to have an impact on the production and decomposition of N_2O
547 (Freing et al., 2012). Our set of simulations highlights that an incomplete representation of the
548 PLF underestimates the expansion of oxygen-depleted waters over the 20 years of simulation
549 in comparison to REF. In climZCST and climZVAR the global volume (0-1000 m) of hypoxic water
550 with [O_2] under 50 mmol m^{-3} is up to 2.3×10^{14} m^3 lower in 2018 compared to that of the control
551 run REF. Thus an incomplete representation of the PLF might lead to an underestimation by 1.2
552 % of the modelled tropical volume of low-oxygenated waters after 20 years.

554 Recent regional studies demonstrated that the interactive PLF strongly affects upwelling
555 systems of the South Pacific and Atlantic oceans (Hernandez et al., 2017; Echevin et al., 2021).
556 Coastal upwellings are known to be sites of high N_2O production with an annual N_2O flux

557 amounting to approximately 20% of the global fluxes while these systems occupy less than 3%
558 of the ocean area (Yang et al., 2020). However, in the present study main modelled
559 perturbations are rather localized over oxygen minimum zones or subtropical gyres (Figure 5;
560 Figure 7). While the latter regional studies were performed at horizontal resolutions compatible
561 with the complex dynamics of coastal upwellings (from 10 km to about 28 km), the resolution
562 of climate models (~1-degree of horizontal resolution) does not allow to resolve these
563 dynamics. A step further would be to evaluate how the sensitivity of N_2O emission to the
564 representation of the PLF depends on the horizontal resolution by running simulations at higher
565 resolution with the same climate model. This would help to better determine how coastal
566 upwelling systems may impact the modelled N_2O inventory through different PLF
567 representations, as well as the associated modelled range of uncertainty.
568
569

570 **Code availability**
571 Sources for NEMO and PISCESv2 codes are available from https://forge.nemo-ocean.eu/nemo.
572

573 **Author contribution**
574 SB, JJ and RS conceptualized this study and its methodology. SB designed the numerical
575 experiments, carried them out and prepared the manuscript with contributions from all co-
576 authors. WL processed OHC data.
577

578 **Competing interests**
579 The authors declare that they have no conflict of interest.
580

581 **Acknowledgements**
582 The OHC data were collected and made freely available by the International Argo Program and
583 the national programs that contribute to it (https://argo.ucsd.edu, https://www.ocean-
584 ops.org). The Argo Program is part of the Global Ocean Observing System. This project has
585 received funding from the European Union's Horizon 2020 research and innovation
586 programme under Grant Agreement No. 101003536 (ESM2025 – Earth System Models for the
587 Future). The authors thank the two reviewers for their constructive comments and suggestions.
588
589

590 **References**
591
592 **Anderson**,W. G., Gnanadesikan, A., Hallberg, R. , Dunne, J., and Samuels, B. L.: Impact of ocean color on
593 the maintenance of the Pacific Cold Tongue, Geophys. Res. Lett., 34, L11609, doi:10.1029/2007GL030100,
594 2007.
595
596 **Asselot**, R., Lunkeit, F., Holden, P. B., and Hense, I.: Climate pathways behind phytoplankton-induced
597 atmospheric warming. Biogeosciences, 19(1), 223-239, 2022.
598
599 **Aumont**, O., Ethé, C., Tagliabue, A., Bopp, L., and Gehlen, M.: PISCES-v2: An ocean biogeochemical model
600 for carbon and ecosystem studies. Geoscientific Model Development, 8, 2465–2513, 2015.
601
602 **Arévalo-Martinez**, D. L., Kock, A. , Steinhoff, T. , Brandt, P. , Dengler, M. , Fischer, T. , Körtzinger, A. , and
603 Bange, H. W. : Nitrous oxide during the onset of the Atlantic cold tongue, J. Geophys. Res. Oceans, 122,
604 171–184, doi:10.1002/2016JC012238, 2017.
605

606 **Arévalo-Martínez**, D. L., Steinhoff, T., Brandt, P., Körtzinger, A., Lamont, T., Rehder, G., and Bange, H. W.:
607 N2O emissions from the northern Benguela upwelling system. Geophysical Research Letters, 46, 3317–
608 3326. https://doi.org/10.1029/2018GL081648, 2019.
609
610 **Berthet**, S., Séférian, R., Bricaud, C., Chevallier, M., Voldoire, A., and Ethé, C.: Evaluation of an online grid-
611 coarsening algorithm in a global eddy-admitting ocean biogeochemical model. Journal of Advances in
612 Modeling Earth Systems, 11, 1759–1783. https://doi.org/10.1029/2019MS001644, 2019.
613
614 **Bopp**, L., Resplandy, L., Orr, J. C., Doney, S. C., Dunne, J. P., Gehlen, M., Halloran, P., Heinze, C., Ilyina, T.,
615 Séférian, R., Tjiputra, J., and Vichi, M.: Multiple stressors of ocean ecosystems in the 21st century:
616 projections with CMIP5 models, Biogeosciences, 10, 6225–6245, doi:10.5194/bg-10-6225-2013, 2013.
617
618 **Bricaud**, A., Babin, M., Morel, A., and Claustre, H.: Variability in the chlorophyll-specific absorption
619 coefficients of natural phytoplankton: analysis and parameterization, J. Geophys. Res., 100, 13321–13332,
620 1995.
621
622 **Cheng**, L., Trenberth, K. E., Palmer, M. D., Zhu, J., and Abraham, J. P.: Observed and simulated full-depth
623 ocean heat-content changes for 1970–2005, Ocean Sci., 12, 925–935, https://doi.org/10.5194/os-12-925-
624 2016, 2016.
625
626 **Cocco**, V., Joos, F., Steinacher, M., Frölicher, T. L., Bopp, L., Dunne, J., Gehlen, M., Heinze, C., Orr, J.,
627 Oschlies, A., Schneider, B., Segschneider, J., and Tjiputra, J.: Oxygen and indicators of stress for marine life
628 in multi-model global warming projections, Biogeosciences, 10, 1849–1868, doi:10.5194/bg-10-1849-2013,
629 2013.
630
631 **Echevin**, V., Hauschildt, J., Colas, F., Thomsen, S., and Aumont, O.: Impact of chlorophyll shading on the
632 Peruvian upwelling system. Geophysical Research Letters, 48, e2021GL094429.
633 https://doi.org/10.1029/2021GL094429, 2021.
634
635 **Edwards**, A. M., Wright, D. G., and Platt, T.: Biological heating effect of a band of phytoplankton. *Journal of*
636 *Marine Systems*, 49, 89-103. doi: 10.1016/j.jmarsys.2003.05.011, 2004.
637
638 **Edwards**, A. M., Platt, T., and Wright, D. G.: Biologically induced circulation at fronts. *Journal of geophysical*
639 *research*, 49, 89-103. doi: 10.1016/j.jmarsys.2003.05.011, 2001.
640
641 **Eppley**, R. W.: Temperature and phytoplankton growth in the sea, Fish. Bull., 70, 1063–1085, 1972.
642
643 **Freing**, A., Wallace, D. W. R., and Bange, H. W.: Global oceanic production of nitrous oxide. Philos. Trans. R.
644 Soc. London Ser. B, **367**, 1245–1255, 2012.
645
646 **Garcia**, H. E., Locarnini, R. A., Boyer, T. P., Antonov, J. I., Baranova, O.K., Zweng, M.M., Reagan, J.R., and
647 Johnson, D.R.: World Ocean Atlas 2013, Volume 3: Dissolved Oxygen, Apparent Oxygen Utilization, and
648 Oxygen Saturation. S. Levitus, Ed., A. Mishonov Technical Ed.; NOAA Atlas NESDIS 75, 27 pp, 2014.
649
650 **Gildor**, H., and Naik, N. H.: Evaluating the effect of interannual variations of surface chlorophyll on upper
651 ocean temperature, J. Geophys. Res., 110, C07012, doi:10.1029/2004JC002779, 2005.
652
653 **Gnanadesikan**, A., and Anderson, W. G.: Ocean water clarity and the ocean general circulation in a coupled
654 climate model, J. Phys. Ocean., 39, 314–332, 2009.
655
656 **Good**, S. A., Martin, M. J., and Rayner, N. A.: EN4: quality controlled ocean temperature and salinity profiles
657 and monthly objective analyses with uncertainty estimates, Journal of Geophysical Research: Oceans,
658 doi:10.1002/2013JC009067, 2013.
659

Hajima, T., Watanabe, M., Yamamoto, A., Tatebe, H., Noguchi, M. A., Abe, M., Ohgaito, R., Ito, A., Yamazaki, D., Okajima, H., Ito, A., Takata, K., Ogochi, K., Watanabe, S., and Kawamiya, M.: Development of the MIROC-ES2L Earth system model and the evaluation of biogeochemical processes and feedbacks, Geosci. Model Dev., 13, 2197–2244, https://doi.org/10.5194/gmd-13-2197-2020, 2020.

Heinze, C., T. Blenckner, H. Martins, D. Rusiecka, R. Döscher, M. Gehlen, N. Gruber, E. Holland, Ø. Hov, F. Joos, J. B. R. Matthews, R. Rødven and S. Wilson: The quiet crossing of ocean tipping points, Proceedings of the National Academy of Sciences, 118 (9) e2008478118; DOI: 10.1073/pnas.2008478118, 2021.

Hernandez, O., Jouanno, J., Echevin, V., and Aumont, O.: Modification of sea surface temperature by chlorophyll concentration in the Atlantic upwelling systems, J. Geophys. Res. Oceans, 122, 5367–5389, doi:10.1002/2016JC012330, 2017.

Hutchins, D.A., and Capone, D.G: The marine nitrogen cycle: new developments and global change. Nat. Rev. Microbiol., https://doi-org.insu.bib.cnrs.fr/10.1038/s41579-022-00687-z, 2022.

Ilyina, T., Six, K. D. , Segschneider, J., Maier-Reimer, E., Li, H., and Núñez-Riboni, I.: Global ocean biogeochemistrymodel HAMOCC: Model architecture and performance as component of the MPI-Earth system model in different CMIP5 experimental realizations,J.Adv.Model.EarthSyst.,5, 287–315, doi:10.1029/2012MS000178, 2013.

IPCC: Summary for Policymakers, in: IPCC Special Report on the Ocean and Cryosphere in a Changing Climate, edited by: Pörtner,H.-O., Roberts, D.C., Masson-Delmotte, V., Zhai, P., Tignor, M., Poloczanska, E., Mintenbeck, K., Nicolai, M., Okem, A., Petzold, J., Rama, B., and Weyer, N., 2019.

Ji, Q., Babbin, A. R., Jayakumar, A., Oleynik, S., and Ward, B. B.: Nitrous oxide production by nitrification and denitrification in the Eastern Tropical South Pacific oxygen minimum zone, Geophys. Res. Lett., 42, 10,755–10,764, doi:10.1002/2015GL066853, 2015.

Ji, Q., Buitenhuis, E., Suntharalingam, P., Sarmiento, J. L., and Ward, B. B. Global nitrous oxide production determined by oxygen sensitivity of nitrification and denitrification. Global Biogeochemical Cycles, 32, 1790–1802. https://doi.org/10.1029/2018GB005887, 2018.

Kahru, M., Leppaenen, J.-M., and Rud, O.: Cyanobacterial blooms cause heating of the sea surface, Mar. Ecol.-Prog. Ser., 101, 1–7, 1993.

Kolodziejczyk, N., Llovel, W., and Portela, E.: Interannual variability of upper ocean water masses as inferred from Argo Array, Journal of Geophysical Research: Oceans. doi:10.1029/2018JC014866, 2019.

Kolodziejczyk, N., Prigent-Mazella, A., and Gaillard, F.: ISAS temperature and salinity gridded fields. SEANOE. https://doi.org/10.17882/52367, 2021.

Kortzinger, A., Hedges, J. I., and Quay, P. D.: Redfield ratios revisited: removing the biasing effect of anthropogenic CO2, Limnol. Oceanogr., 46, 964–970, 2001.

Kwiatkowski, L., Torres, O., Bopp, L., Aumont, O., Chamberlain, M., Christian, J. R., Dunne, J. P., Gehlen, M., Ilyina, T., John, J. G., Lenton, A., Li, H., Lovenduski, N. S., Orr, J. C., Palmieri, J., Santana-Falcón, Y., Schwinger, J., Séférian, R., Stock, C. A., Tagliabue, A., Takano, Y., Tjiputra, J., Toyama, K., Tsujino, H., Watanabe, M., Yamamoto, A., Yool, A., and Ziehn, T.: Twenty-first century ocean warming, acidification, deoxygenation, and upper-ocean nutrient and primary production decline from CMIP6 model projections, Biogeosciences, 17, 3439–3470, https://doi.org/10.5194/bg-17-3439-2020, 2020.

Lam, P., and Kuypers, M.: Microbial Nitrogen Cycling Processes in Oxygen Minimum Zones, Annual Review of Marine Science 3:1, 317-345, doi:10.1146/annurev-marine-120709-142814, 2011.

714

715 **Large**, W. G., and Yeager, S.: The global climatology of an interannually varying air-sea ux data set, Clim.
716 Dyn., 33, 341–364, doi:10.1007/s00382-008-0441-3, 2009.

717

718 **Lengaigne**, M., Madec, G., Bopp, L., Menkes, C., Aumont, O., and Cadule, P.: Bio-physical feedbacks in the
719 Arctic Ocean using an Earth system model, Geophys. Res. Lett., 36, L21602, doi:10.1029/2009GL040145,
720 2009.

721

722 **Lengaigne**, M., Menkes, C., Aumont, O., Gorgues, T., Bopp, L., André, J.-M., and Madec, G.: Influence of the
723 oceanic biology on the tropical Pacific climate in a coupled general circulation model. Clim. Dyn., 28, 503–
724 516, https://doi.org/10.1007/s00382-006-0200-2, 2007.

725

726 **Levitus**, S., Antonov, J. I. , Boyer, T. P., Baranova, O. K., Garcia, H. E., Locarnini, R. A., Mishonov, A.V.,
727 Reagan, J. R., Seidov, D., Yarosh, E. S., and Zweng, M. M.: World Ocean heat content and thermosteric sea
728 level change (0-2000 m) 1955-2010. Geophys. Res. Lett. , 39, L10603, doi:10.1029/2012GL051106, 2012.

729

730 **Liang**, X., Liu, C. R., Ponte, M., and Chambers, D. P.: A Comparison of the Variability and Changes in Global
731 Ocean Heat Content from Multiple Objective Analysis Products During the Argo Period, J. Climate, 34(19),
732 7875–7895, https://doi.org/10.1175/JCLID-20-0794.1, 2021.

733

734 **Llovel**, W., and Terray, L.: Observed southern upper-ocean warming over 2005–2014 and associated
735 mechanisms, Environ. Res. Lett., 11, 124023, 2016.

736

737 **Llovel**, W., Kolodziejczyk, N., Close, S., Penduff, T., Molines, J.-M., and Terray, L.: Imprint of intrinsic ocean
738 variability on decadal trends of regional sea level and ocean heat content using synthetic profiles, Environ.
739 Res. Lett., 17, 044063, 2022.

740

741 **Locarnini**, R. A., Mishonov, A. V., Antonov, J. I., Boyer, T. P., Garcia, H. E., Baranova, O. K., Zweng, M. M.,
742 Paver, C. R., Reagan, J. R., Johnson, D. R., Hamilton, M., and Seidov, D.: World Ocean Atlas 2013, Volume 1:
743 Temperature. S. Levitus, Ed., A. Mishonov Technical Ed.; NOAA Atlas NESDIS 73, 40 pp, 2013.

744

745 **Löptien**, U., Eden, C., Timmermann, A., and Dietze, H.: Effects of biologically induced differential heating in
746 an eddy-permitting coupled ocean-ecosystem model, J. Geophys. Res., 114, C06011,
747 doi:10.1029/2008JC004936, 2009.

748 **Lyman**, J. M., Good, S. A., Gouretski, V. V., Ishii, M., Johnson, G. C., Palmer, M. D., Smith, D. M., and Willis, J.
749 K.: Robust warming of the global upper ocean. Nature **465**, 334–337,
750 https://doi.org/10.1038/nature09043, 2010.

751 **Madec**, G.: Nemo ocean engine. Note du Pôle de modélisation de l'Institut Pierre-Simon Laplace, 27, 1–217,
752 2008.

753

754 **Maes**, C., and O'Kane, T. J.: Seasonal variations of the upper ocean salinity stratification in the Tropics, J.
755 Geophys. Res. Oceans, 119, 1706–1722, doi:10.1002/2013JC009366, 2014.

756

757 **Manizza**, M., Le Quéré, C., Watson, A. J., and Buitenhuis, E. T.: Bio-optical feedbacks among phytoplankton,
758 upper ocean physics and sea-ice in a global model, Geophys. Res. Lett., 32, L05603,
759 doi:10.1029/2004GL020778, 2005.

760

761 **Manizza**, M., Le Quéré, C., Watson, A. J., and Buitenhuis, E. T.: Ocean biogeochemical response to
762 phytoplankton-light feedback in a global model, J. Geophys. Res., 113, C10010, doi:10.1029/2007JC004478,
763 2008.

764

765 **Martinez-Rey**, J., Bopp, L., Gehlen, M., Tagliabue, A., and Gruber, N.: Projections of oceanic N_2O emissions
766 in the 21st century using the IPSL Earth system model, Biogeosciences, 12, 4133–4148,
767 https://doi.org/10.5194/bg-12-4133-2015, 2015.
768
769 **Marzeion**, B., Timmermann, A., Murtugudde, R., and Jin, F.: Biophysical Feedbacks in the Tropical Pacific,
770 Journal of Climate, 18(1), 58-70, 2005
771
772 **Meyssignac** B., Boyer, T., Zhao, Z., Hakuba, M. Z., Landerer, F. W., Stammer, D., Köhl, A., Kato, S., L'Ecuyer,
773 T., Ablain, M., Abraham, J. P., Blazquez, A., Cazenave, A., Church, J. A., Cowley, R., Cheng, L., Domingues, C.
774 M., Giglio, D., Gouretski, V., Ishii, M., Johnson, G. C., Killick, R. E., Legler, D., Llovel, W., Lyman, J., Palmer, M.
775 D., Piotrowicz, S., Purkey, S. G., Roemmich, D., Roca, R., Savita, A., von Schuckmann, K., Speich, S.,
776 Stephens, G., Wang, G., Wijffels, S. E. and Zilberman, N.: Measuring Global Ocean Heat Content to Estimate
777 the Earth Energy Imbalance. Front. Mar. Sci. 6:432. doi: 10.3389/fmars.2019.00432, 2019.
778
779 **Mignot**, J., Swingedouw, D., Deshayes, J., Marti, O., Talandier, C., Séférian, R., Lengaigne, M., and Madec,
780 G.: On the evolution of the oceanic component of the IPSL climate models from CMIP3 to CMIP5: A mean
781 state comparison, Ocean Modelling, Volume 72, Pages 167-184, ISSN 1463-5003,
782 https://doi.org/10.1016/j.ocemod.2013.09.001, 2013.
783
784 **Morel,** A.: Optical modeling of the upper ocean in relation to its biogenous matter content (Case I waters). J
785 Geophys Res 93:10749–10768, 1988.
786
787 **Morel**, A., and Berthon, J.-F.: Surface pigments, algal biomass profiles, and potential production of the
788 euphotic layer : Relationships reinvestigated in view of remote-sensing applications. Limnol. Oceanogr.,
789 34(8), 1545–1562, 1989.
790
791 **Morel,** A., and Maritorena, S.: Bio-optical properties of oceanic waters: a reappraisal. J Geophys Res
792 106:7163–7180, 2001.
793
794 **Murtugudde**, R., Beauchamp, J., McClain, C. R., Lewis, M., and Busalacchi, A. J.: Effects of Penetrative
795 Radiation on the Upper Tropical Ocean Circulation, Journal of Climate, 15(5), 470-486, 2002.
796
797 **Myhre**, G., Shindell, D., Bréon, F.-M., Collins, W., Fuglestvedt, J., Huang, J., Koch, D., Lamarque, J.-F., Lee, D.,
798 Mendoza, B., Nakajima, T., Robock, A., Stephens, G., Takemura, T., and Zhang, H.: Anthropogenic and
799 Natural Radiative Forcing. In: Climate Change 2013: The Physical Science Basis. Contribution of Working
800 Group I to the Fifth Assessment Report of the Intergovernmental Panel on Climate Change [Stocker, T.F., D.
801 Qin, G.-K. Plattner, M. Tignor, S.K. Allen, J. Boschung, A. Nauels, Y. Xia, V. Bex and P.M. Midgley (eds.)].
802 Cambridge University Press, Cambridge, United Kingdom and New York, NY, USA, 2013.
803
804 **Nakamoto**, S., Kumar, S. P., Oberhuber, J. M., Ishizaka, J., Muneyama, K., and Frouin, R.: Response of the
805 equatorial Pacific to chlorophyll pigment in a mixed layer isopycnical ocean general circulation model,
806 Geophys. Res. Lett., 28, 2021– 2024, 2001.
807
808 **Oschlies**, A.: Feedbacks of biotically induced radiative heating on upper-ocean heat budget, circulation, and
809 biological production in a coupled ecosystem-circulation model, J. Geophys. Res., 109, C12031,
810 doi:10.1029/2004JC002430, 2004.
811
812 **Park**, J.-Y., Kug, J.-S., Seo, H., and Bader, J.: Impact of bio-physical feedbacks on the tropical climate in
813 coupled and uncoupled GCMs. Clim Dyn **43,** 1811–1827, https://doi.org/10.1007/s00382-013-2009-0,
814 2014.
815
816 **Patara**, L., Vichi, M., Masina, S., Fogli, P. G., and Manzini, E.: Global response to solar radiation absorbed by
817 phytoplankton in a coupled climate model. Clim Dyn **39,** 1951–1968, https://doi.org/10.1007/s00382-012-
818 1300-9, 2012.

819

820 **Ravishankara**, A. R., Daniel, J. S., and Portmann, R. W.: Nitrous oxide (N2O): The dominant ozone-depleting
821 substance emitted in the 21st century. Science, **326**, 123–125, 2009.

822

823 **Roemmich**, D., and Gilson, J.: The 2004–2008 mean and annual cycle of temperature, salinity, and steric
824 height in the global ocean from the Argo Program. Prog. Oceanogr., 82, 81–100,
825 https://doi.org/10.1016/j.pocean.2009.03.004, 2009.

826

827 **Sallée**, J.-B., Pellichero, V., Akhoudas, C., Pauthenet, E., Vignes, L., Schmidtko, S., Garabato, A. N.,
828 Sutherland, P., and Kuusela, M.: Summertime increases in upper-ocean stratification and mixed-layer
829 depth. Nature 591, 592–598. https://doi.org/10.1038/s41586-021-03303-x, 2021.

830

831 **Schmidtko**, S., Stramma, L., and Visbeck, M.: Decline in global oceanic oxygen content during the past five
832 decades. Nature 542, 335–339, 2017.

833

834 **Séférian**, R., Berthet, S., Yool, A., Palmiéri, J., Bopp, L., Tagliabue, A., Kwiatkwski, L., Aumont, O., Christian,
835 J., Dunne, J., Gehlen, M., Ilyina, T., John, J. G., Li, H., Long, M. C., Luo, J. Y., Nakano, H., Romanou, A.,
836 Schwinger, J., Stock, C., Santana-Falcon, Y., Takano, Y., Tjiputra, J., Tsujino, H., Watanabe, M., Wu, F., and
837 Yamamoto, A.: Tracking Improvement in Simulated Marine Biogeochemistry Between CMIP5 and CMIP6.
838 Curr Clim Change Rep **6,** 95–119, https://doi.org/10.1007/s40641-020-00160-0, 2020.

839

840 **Séférian**, R., Nabat, P., Michou, M., Saint-Martin, D., Voldoire, A., Colin, J., Decharme, B., Delire, C., Berthet,
841 S., Chevallier, M., Sénési, S., Franchisteguy, L., Vial, J., Mallet, M., Joetzer, E., Geoffroy, O., Guérémy, J.-F.,
842 Moine, M.-P., Msadek, R., Ribes, A., Rocher, M., Roehrig, R., Salas-y-Mélia, D., Sanchez, E., Terray, L.,
843 Valcke, S., Waldman, R., Aumont, O., Bopp, L., Dehayes, J., Ethé, C., and Madec, G.: Evaluation of CNRM
844 Earth-System model, CNRM-ESM2-1: role of Earth system processes in present-day and future climate.
845 Journal of Advances in Modeling Earth Systems, 11. https://doi.org/10.1029/2019MS001791, 2019.

846

847 **Sweeney**, C., Gnanadesikan, A., Griffies, S. M., Harrison, M. J., Rosati, A. J., and Samuels, B. L.: Impacts of
848 Shortwave Penetration Depth on Large-Scale Ocean Circulation and Heat Transport, Journal of Physical
849 Oceanography, 35(6), 1103-1119, 2005.

850

851 **Takahashi**, T., Broecker, W. S., and Langer, S.: Redfield ratio based on chemical data from isopycnal
852 surfaces, J. Geophys. Res., 90, 6907–6924, 1985.

853

854 **Tian**, H., Xu, R., Canadell, J.G., Thompson, R. L., Winiwarter, W., Suntharalingam, P., Davidson, E. A., Ciais,
855 P., Jackson, R. B., Janssens-Maenhout, G., Prather, M. J., Regnier, P., Pan, N., Pan, S., Peters, G., Shi, H.,
856 Tubiello, F. N., Zaehle, S., Zhou, F., Arneth, A., Battaglia, G., Berthet, S., Bopp, L., Bouwman, A. F.,
857 Buitenhuis, E. T., Chang, J., Chipperfield, M. P., Dangal, S. R. S., Dlugokencky, E., Elkins, J., Eyre, B. D., Fu, B.,
858 Hall, B., Ito, A., Joos, F., Krummel, P. B., Landolfi, A., Laruelle, G. G., Lauerwald, R., Li, W., Lienert, S.,
859 Maavara, T., MacLeod, M., Millet, D. B., Olin, S., Patra, P. K., Prinn, R. G., Raymond, P. A., Ruiz, D. J., van der
860 Werf, G. R., Vuichard, N., Wang, J. , Weiss, R., Wells, K. C., Wilson, C., Yang, J., and Yao, Y.: A comprehensive
861 quantification of global nitrous oxide sources and sinks. Nature 586, 248–256,
862 https://doi.org/10.1038/s41586-020-2780-0, 2020.

863

864 **Tiano**, L., Garcia-Robledo, E., Dalsgaard, T., Devol, A. H., Ward, B. B., Ulloa, O., Canfield, D. E., and Revsbech,
865 N. P.: Oxygen distribution and aerobic respiration in the north and south eastern tropical Pacific oxygen
866 minimum zones. Deep Sea Research Part I: Oceanographic Research Papers, Volume 94, Pages 173-183,
867 https://doi.org/10.1016/j.dsr.2014.10.001, 2014.

868

869 **Timmermann**, A., and Jin, F.-F.: Phytoplankton influences on tropical climate, Geophys. Res. Lett., 29(23),
870 2104, doi:10.1029/2002GL015434, 2002.

871

872 **Tsujino**, H., Urakawa, S., Nakano, H., Small, R. J., Kim, W. M., Yeager, S. G., Danabasoglu, G., Suzuki, T.,
873 Bamber J. L., Bentsen, M., Böning, C. W., Bozec, A., Chassignet, E. P., Curchitser, E., Boeira Dias, F., Durack,
874 P. J., Griffies, S. M., Harada, Y., Ilicak, M., Josey, S. A., Kobayashi, C., Kobayashi, S., Komuro, Y., Large, W. G.,
875 Le Sommer, J., Marsland, S. J., Masina, S., Scheinert, M., Tomita, H., Valdivieso, M., and Yamazaki, D.: JRA-
876 55 based surface dataset for driving ocean–sea-ice models (JRA55-do), Ocean Model., 130, 79–139,
877 https://doi.org/10.1016/j.ocemod.2018.07.002, 2018.

879 **Tsujino**, H., Urakawa, L. S., Griffies, S. M., Danabasoglu, G., Adcroft, A. J., Amaral, A. E., Arsouze, T., Bentsen,
880 M., Bernardello, R., Böning, C. W., Bozec, A., Chassignet, E. P., Danilov, S., Dussin, R., Exarchou, E., Fogli, P.
881 G., Fox-Kemper, B., Guo, C., Ilicak, M., Iovino, D., Kim, W. M., Koldunov, N., Lapin, V., Li, Y., Lin, P., Lindsay,
882 K., Liu, H., Long, M. C., Komuro, Y., Marsland, S. J., Masina, S., Nummelin, A., Rieck, J. K., Ruprich-Robert, Y.,
883 Scheinert, M., Sicardi, V., Sidorenko, D., Suzuki, T., Tatebe, H., Wang, Q., Yeager, S. G., and Yu, Z. (2020).
884 Evaluation of global ocean–sea-ice model simulations based on the experimental protocols of the Ocean
885 Model Intercomparison Project phase 2 (OMIP-2), Geosci. Model Dev., 13, 3643–3708,
886 https://doi.org/10.5194/gmd-13-3643-2020, 2020.

888 **Uitz**, J., Claustre, H., Morel, A., and Hooker, S. B.: Vertical distribution of phytoplankton communities in
889 open ocean: An assessment based on surface chlorophyll, *J. Geophys. Res.*, 111, C08005,
890 doi:10.1029/2005JC003207, 2006.

892 **Valente**, A., Sathyendranath, S., Brotas, V., Groom, S., Grant, M., Taberner, M., Antoine, D., Arnone, R.,
893 Balch, W., Barker, K., Barlow, R., Bélanger, S., Berthon, J. F., Besiktepe, S., Brando, V., Canuti, E., Chavez, F.,
894 Claustre, H., Crout, R., Frouin, R., Garcìa-Soto, C., Gibb, S. W., Gould, R., Hooker, S., Kahru, M., Klein, H.,
895 Kratzer, S, Loisel, H., McKee, D., Mitchell, B. G., Moisan, T., Muller-Karger, F., O'Dowd, L., Ondrusek, M.,
896 Poulton, A, Repecaud, M., Smyth, T., Sosik, H. M., Twardowski, M., Voss, K., Werdell, J., Wernand, M., and
897 Zibordi, G.: A compilation of global bio-optical in situ data for ocean-colour satellite applications. Earth Syst.
898 Sci. Data, 8, 235–252, doi: 10.5194/essd-8-235-2016, 2016.

900 **Wanninkhof**, R.: Relationship between wind speed and gas exchange over the ocean, J. Geophys. Res., 97,
901 7373–7382, doi:10.1029/92JC00188, 1992.

903 **Wanninkhof**, R.: Relationship between wind speed and gas exchange over the ocean revisited, Limnol.
904 Oceanogr. Methods, 12, doi:10.4319/lom.2014.12.351, 2014.

906 **Weiss**, R. F., and Price, B. A. : Nitrous oxide solubility in water and seawater Marine Chemistry, Volume 8,
907 Issue 4, Pages 347-359; DOI: 10.1016/0304-4203(80)90024-9, 1980.

909 **Wilson**, S. T., Al-Haj, A. N., Bourbonnais, A., Frey, C., Fulweiler, R. W., Kessler, J. D., Marchant, H. K., Milucka,
910 J., Ray, N. E., Suntharalingam, P., Thornton, B. F., Upstill-Goddard, R. C., Weber, T. S., Arévalo-Martínez, D.
911 L., Bange, H. W., Benway, H. M., Bianchi, D., Borges, A. V., Chang, B. X., Crill, P. M., del Valle, D. A., Farías, L.,
912 Joye, S. B., Kock, A., Labidi, J., Manning, C. C., Pohlman, J. W., Rehder, G., Sparrow, K. J., Tortell, P. D.,
913 Treude, T., Valentine, D. L., Ward, B. B., Yang, S., and Yurganov, L. N.: Ideas and perspectives: A strategic
914 assessment of methane and nitrous oxide measurements in the marine environment, Biogeosciences, 17,
915 5809–5828, https://doi.org/10.5194/bg-17-5809-2020, 2020.

917 **Yang**, S., Chang, B. X.,Warner, M. J., Weber, T. S., Bourbonnais, A. M., Santoro, A. E., Kock, A., Sonnerup, R.
918 E., Bullister, J. L., Wilson, S. T., and Bianchi, D.: Global reconstruction reduces the uncertainty of oceanic
919 nitrous oxide emissions and reveals a vigorous seasonal cycle, Proceedings of the National Academy of
920 Sciences, 117 (22) 11954-11960; DOI: 10.1073/pnas.1921914117, 2020.
921